Article

Aerodynamic Performance and Wake Characteristics Analysis of Archimedes Spiral Wind Turbine Rotors with Different Blade Angle

Ke Song [1,2,*] **, Huiting Huan** [3] **and Yuchi Kang** [4]

1 School of Mechanical and Electrical Engineering, Kunming University, Kunming 650214, China
2 Shen Weiming Academician Workstation of Intelligent Manufacturing Technology in Yunnan (Kunming), Kunming University, Kunming 650214, China
3 School of Mechano-Electronic Engineering, Xidian University, Xi'an 710071, China
4 Faculty of Mechanical and Electrical Engineering, Kunming University of Science and Technology, Kunming 650500, China
* Correspondence: songke@kmu.edu.cn

Abstract: Continuous improvement of wind turbines represent an effective way of achieving green energy and reducing dependence on fossil fuel. Conventional lift-type horizontal axis wind turbines, which are widely used, are designed to run under high wind speed to obtain a high efficiency. Aiming to use the low-speed wind in urban areas, a novel turbine, which is called the Archimedes Spiral Wind Turbine (abbreviated as ASWT), was recently proposed for low-speed wind applications. In the current work, a numerical simulation on the five ASWT rotors with different blade angles was carried out, which were performed to predict the detailed aerodynamic performance and wake characteristics. The results show that the ASWT rotor with a large blade angle has a wider operating tip speed ratio range and a higher tip speed ratio point of maximum power coefficient within a certain range, and yet the ASWT rotor with the larger blade angle has a higher thrust coefficient. Additionally, the ASWT rotor with a large blade angle usually has a large power coefficient and thrust coefficient fluctuation amplitude. On the other hand, the ASWT rotor with a small blade angle permits the undisturbed free stream to pass through the rotor blades more easily than that with a large blade angle. This causes a stronger blockage effect for the ASWT rotor with a large blade angle. Moreover, the blade angle also has a great effect on the shape of the vortex structure. The blade tip vortex of the fixed-angle ASWT rotors is more stable than those of the variable-angle ASWT rotors. The hub vortex of the ASWT rotors with a large blade angle is stronger than those with a small blade angle. Meanwhile, the wake recovery for ASWT rotors with a small blade angle is evidently lower than those with a large blade angle.

Keywords: wind energy; ASWT rotor; aerodynamic performance; wake characteristics; blade angle

1. Introduction

Fossil fuels have brought a lot of problems such as environmental pollution, climate change and global warming. As an excellent alternative to traditional fossil fuels, wind energy has been in the spotlight in recent years as a clean and carbon-free energy source [1,2]. The total amount of proven and probable wind power reserves is approximately 20 million megawatts, which is far beyond the hydropower reserves [3–5]. To date, the wind turbine is considered to be the most promising wind energy technology. According to the operation mode, there are the horizontal axis wind turbine (HAWT) and vertical axis wind turbine (VAWT) [6,7], and the HAWT has the highest efficiency and is considered to possess the most successful commercial applications [8,9]. On the other hand, the wind turbine can be classified into lift or drag types depending on the aerodynamic force acting on the blade. The HAWT relies on lift force to produce power, which is known as a lift-type HAWT.

Meanwhile, most of the drag types are VAWT, which are known to be less efficient than the HAWT. However, a HAWT is usually designed to run under a high wind speed (more than 6 m/s) to obtain the highest efficiency [10,11]. In the field of urban areas, such technology is limited due to the low flow rates [12]. To resolve the issue of applications in urban areas, a novel wind turbine, which is called the Archimedes Spiral Wind Turbine (ASWT), was recently proposed. Unlike the HAWT designed based on the Blade Element Momentum (BEM) theory, the ASWT was created based on the Archimedes spiral. The Archimedes spiral is a pattern generated by a moving point which is leaving a fixed point at a constant speed and a constant angular speed. This pattern can be found in general in nature such as in the nautilus, *Thatcheria mirabilis* and low-pressure vortex region shown in Figure 1.

Figure 1. The Archimedes spiral shape in nature.

The ASWT rotor includes three screw blades wrapped around each other and a horizontal shaft parallel to the ground. Although the ASWT and the HAWT are both horizontal-axis types, the biggest difference between them is that the ASWT mainly depends on the drag force to produce power, which makes it a drag-type horizontal axis turbine. In light of this, the aerodynamic force on the ASWT rotor is shown in Figure 2. The wind-induced axial thrust (T) can be separated into two parts. The lift component (T_L) (perpendicular to blade section) creates stress, and the drag component (T_D) (parallel to blade section) produce power. Additionally, according to the characteristics of adrag-type turbine, the ASWT can produce power at low wind speed. In addition, it can automatically align to the wind direction without any yaw equipment due to its unique spiral shape. Therefore, the demand for the AWST has been increasing recently, not only for urban applications, but also for lighting systems in villages [13].

In recent years, relevant investigations on the ASWT rotor's performance have been conducted. Kim et al. [14] used a Computational Fluid Dynamics (CFD) tool with experimental validation to analyze the output power of an ASWT rotor. Safidari [15] tested an ASWT rotor's aerodynamic efficiency through CFD analysis and experiment. Lu et al. [16] used a theoretical model and a CFD tool to study an ASWT rotor's power performance. Jang et al. [17] conducted an experimental test on an ASWT rotor's output power at different wind speed. Nawar et al. [18] analyzed two ASWT rotors' performance using a CFD tool and experimental test. Kamalet al. [19,20] studied aerofoiled profiles, thickness and angle on the ASWT rotor's performance. Nepal et al. [21] designed an ASWT rotor and carried out a CFD simulation on the performance. Mustafa et al. [22] conducted a performance comparison between an ASWT rotor and a propeller. Ozeh et al. [23] experi-

mentally tested an ASWT rotor's output power at low wind speed. Refaie et al. [24] and Hameed et al. [25] used a shroud to increase an ASWT rotor's output power and carried out an optimization design based on CFD analysis.
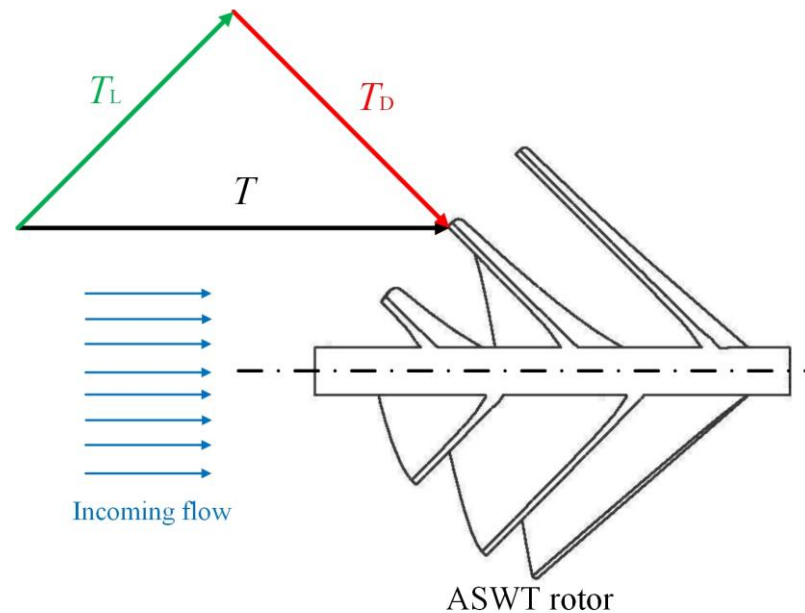

Figure 2. Aerodynamic force analysis on the ASWT rotor.

Literature research shows that a few works on the ASWT rotor have been introduced for the time being. However, the above research mainly focuses on the output power issues, and there are still very few studies aiming at its aerodynamic performance and wake characteristics. Additionally, the effect of the blade angle on the ASWT rotor's performance is not clear so far, and such work is becoming more prominent and necessary for design and application. To this end, the highlights for this work are: (1) intensive numerical studies are performed for five ASWT rotors, (2) the influence of blade angle on the ASWT rotor's aerodynamic performance and wake characteristics is investigated, (3) detailed explanations on the ASWT performance difference are given. The remainder of the present work is structured as follows: Section 2 presents governing equations, aerodynamic coefficients, turbine modeling (including numerical setup and computational domain) and numerical validation. Section 3 presents the results of power and thrust coefficients, pressure distribution, velocity distribution and the vortex structures of the AWSTs in the case study. Finally, Section 4 summarizes the conclusions drawn from the study.

2. Numerical Methods

2.1. General Features

The Reynolds Averaging Navier–Stokes (RANS) equations can be written as:

$$\frac{\partial u_i}{\partial x_i} = 0 \tag{1}$$

$$\frac{\partial}{\partial t}(\rho u_i) + \frac{\partial}{\partial x_j}(\rho u_i u_j) = -\frac{\partial p}{\partial x_i} + \frac{\partial}{\partial x_j}\left(\mu \frac{\partial u_i}{\partial x_j} - \rho \overline{u'_i u'_j}\right) + f_i \tag{2}$$

where u_i is time averaged velocity, p is time average pressure, ρ is fluid density, f_i is body force.

The aerodynamic coefficients of an ASWT, including tip speed ratio (*TSR*), power coefficient (*C_P*) and thrust coefficient (*C_T*) using Equations (3)–(5), respectively.

$$TSR = \frac{\omega R}{V_0} = \frac{\pi n R}{30 V_0} \tag{3}$$

$$C_P = \frac{P}{0.5 \rho A V_0^3} \tag{4}$$

$$C_T = \frac{T}{0.5 \rho A V_0^2} \tag{5}$$

where P is the power output (W) of ASWT, T is the axis thrust (N) of ASWT, V_0 is wind speed (m/s), R is the radius of ASWT rotor, A is the sweep area of ASWT rotor (πR^2, m^2), n is the rotational speed of ASWT rotor (rpm).

2.2. ASWTRotor Model

The main goal of this work is to study the blade angle effects on the aerodynamic performance and the wake characteristics of ASWT rotor. The ASWT rotor has three blades of 125 mm radius fitted to a shaft at an angle of 120°. The radius of ASWT rotor is defined as the vertical distance from the blade-tip at exit to the axis. The shaft has a 25 mm diameter, and the thickness of blades is 3 mm. In addition, the ASWT rotor has three blade angles, while the $\alpha 3$ is defined as the angle between the axis and the first blade's tip at exit, the $\alpha 2$ is defined as the angle between the axis and the second blade based on the same plane as the $\alpha 3$ is measured and the $\alpha 1$ is defined as the angle between the axis and the third blade based on the same plane as the $\alpha 3$ is measured, shown in Figure 3. The geometries were generated by utilizing SolidWorks software (Dassault Systemes Inc., Paris, France). Moreover, according to Nawar et al. [18], an ASWT rotor can be classified into the fixed-angle type and the variable-angle type depending on the blade angle distribution on the rotor. For the fixed-angle type, the blade angles at $\alpha 1$, $\alpha 2$ and $\alpha 3$ are equal. For the variable-angle type, the blade angles gradually increase from $\alpha 1$, $\alpha 2$ and$\alpha 3$. In the present work, the angles of 30°, 45° and 60° based on the reference [17,18,24,25], were chosen to build up the five ASWT rotors with different blade angles, as shown in Figure 4. In a follow-up analysis, to differentiate the ASWT cases with different blade angle values, notation "x-x-x" is applied (e.g., "30-45-60" denotes the case for an ASWT with the $\alpha 1 = 30°$, the $\alpha 2 = 45°$ and the $\alpha 3 = 60°$). It is worth mentioning that the 30-30-30 is the special one which has an additional $\alpha 0$ due to its small blade angle geometric characteristics. Among the five ASWT rotors, the 30-30-30, 45-45-45 and 60-60-60 have a fixed blade angle type, while the 15-30-45 and 30-45-60 have a variable blade angle type.

2.3. CFD Approach and Boundary Conditions

An unsteady CFD approach via the finite-volume method through ANSYS-FLUENT software (Ansys Inc., Canonsburg, PA, USA) was used to assess the performance of ASWT rotor. A Sugon high-performance computing system with XeonE7 (64 cores used) was used for the simulation. The two-equation eddy viscosity SST $k - \omega$ turbulence model [26], which has been widely used for wind turbines or tidal turbines [27–30], was adopted in the present study. The calculation domain, which contains a stationary domain and a rotatory domain, and the defined coordinate system are shown in Figure 5. The ASWT is located in the rotatory domain, and the stationary domain is under the action of the incoming wind. The rotatory domain was set as a cylinder to define the rotation of the ASWT rotor relative to the stationary domain; thereby, a relative slip between the interfaces and the flow field information is transmitted. The length and diameter of the rotatory domain are slightly larger than the ASWT rotor shaft and diameter. A uniform wind speed (V_0) of 5.0 m/s was applied at the velocity inlet, and the outlet was set as outflow. The ASWT rotor's center is placed at 5 D distance from the inlet and a 10 D distance from the outflow with a blockage

ratio of <1%. Additionally, the ASWT rotor used a non-slip condition. The surrounding boundary of the stationary domain used a free-slip condition.
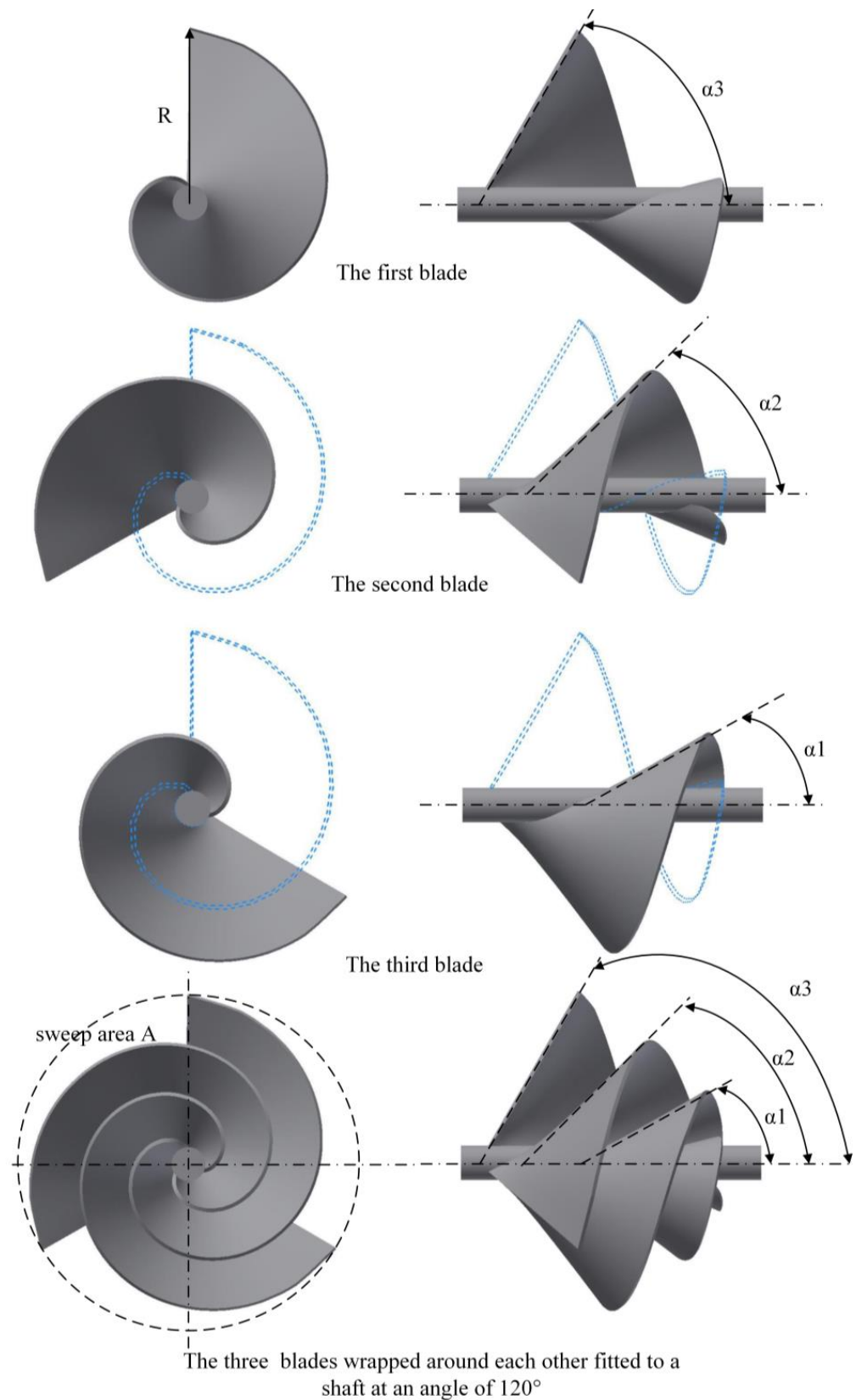

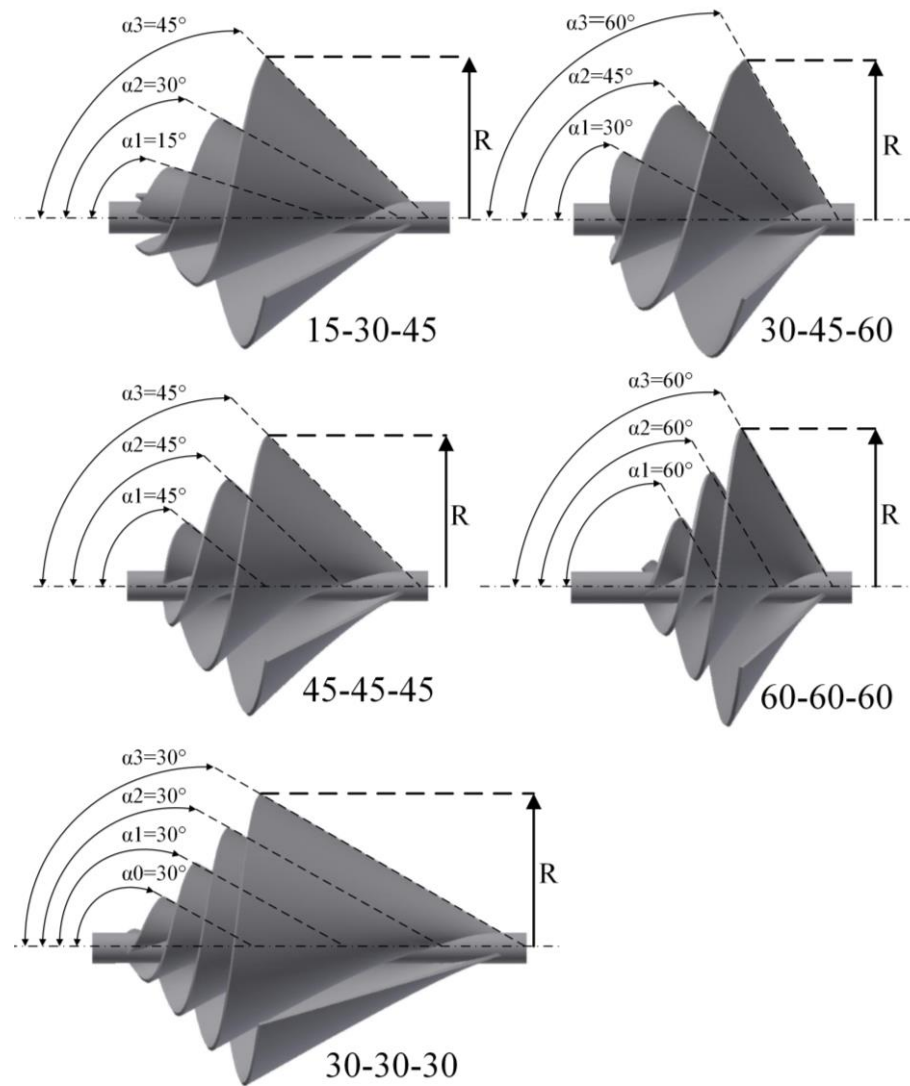**Figure 3.** Definition of the blade angle on an ASWT rotor.

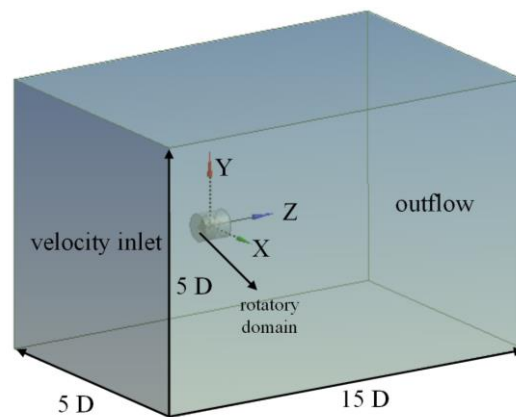**Figure 4.** Schematic view of the five ASWT rotors.

Figure 5. Calculation domain.

2.4. Mesh Generation and Calculation Setups

A suitable mesh is essential to the accuracy of simulation results. The computational domain (including stationary domain and rotatory domain) was completely created and meshed using an unstructured mesh. As the ASWT rotor is complex, the grid of the rotor

surface and rotatory domain was further refined. The boundary layer meshes (including eight separate layers) were used to cover the surface of ASWT rotor. Assuming the reference length is ASWT rotor diameter, and the reference speed is 5.0 m/s, the system has a Reynolds number of 8.4×10^4. In order to meet the requirements of the SST $k - \omega$ turbulence model, the amount of Y+ around the surface was set as Y+ = 1, which is equal to 5.4×10^{-5} m. Figure 6 shows the mesh detail on the surface and near the central *x-y* plane of an ASWT rotor. Additionally, to ensure mesh-independency (taking the 30-45-60 at TSR = 1.5 as examples), three different sets of mesh cell numbers of 3,213,540, 5,429,876 and 8,327,596 have been employed, shown in Table 1. The power coefficient and thrust coefficient defined in Section 2.1 were selected as the determining factor in the mesh independence assessment. The power coefficient and thrust coefficient obtained using the medium mesh varied by 2.18% and 0.59%, respectively, compared to the coarse mesh, and those obtained using the fine mesh varied by 0 and 0.44%, respectively, compared to the medium mesh. Consequently, according to the deviation and the calculation time, the mesh set with 5,429,876 cell numbers was selected to perform the numerical simulations for the subsequent calculations. It is worth mentioning that the mesh cell numbers for the five ASWT cases in this work are basically consistent. In the present study, approximately 11,500 interactions were found to be adequate for an unsteady ASWT case numerical solution. Each case consumed approximately 550 core hours to finish the calculation process.
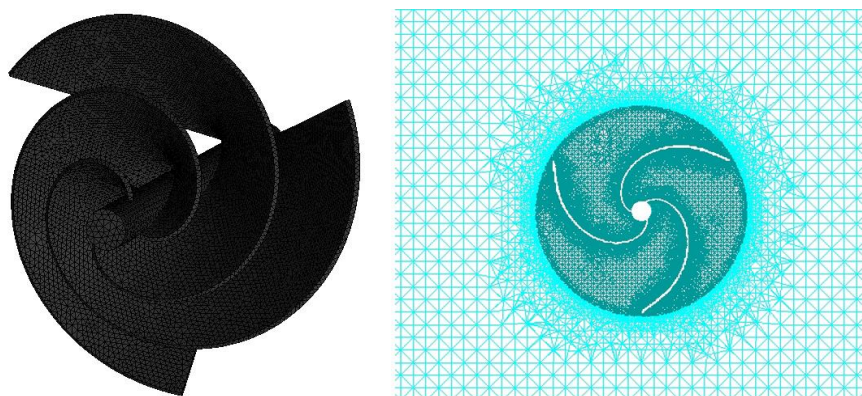

Figure 6. Mesh distribution on the surface and near the central *x-y* plane of ASWT rotor.

Table 1. Mesh independence assessment.

Mesh Density	Total Cells	C_P	C_T
Coarse	3,213,540	0.229	0.673
Medium	5,429,876	0.234	0.677
Fine	8,327,596	0.234	0.680

2.5. Numerical Model Validation

To verify the present CFD method, a comparison between the 30-45-60 ASWT rotor's C_P obtained from the CFD simulation and the experimental data reported by Kamal et al. [20] was carried out. The 30-45-60 ASWT rotor was experimentally tested in a wind tunnel lab, at the Helwan University, Egypt, over a range of TSR from 0.5 to 3.0. The experiment devices include a rotational speed sensor for rotor rotational speed measurements with accuracy ±5%, a turbine meter for wind velocity measurements, a rotating torque sensor for rotor torque measurements within accuracy ±2%, a laptop for data processing and a wind tunnel system for providing air flow in the speed range of 6 m/s to 12 m/s. By monitoring the rotational speed reading values and the torque reading values, the C_P have been computed and measured, as shown in Figure 7. Despite the fact that some deviation existed, overall, the CFD value agrees with the experimental value shown in Figure 8. The

maximum and the second largest relative error are 16% and 10% (the far right and the far left experiment points), the other points' relative error are less than 6%, which indicates that the CFD method adopted in current work can predict the results with acceptable accuracy.
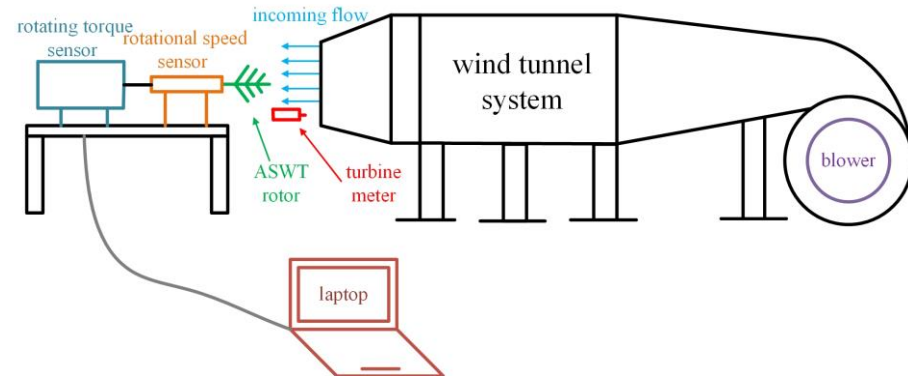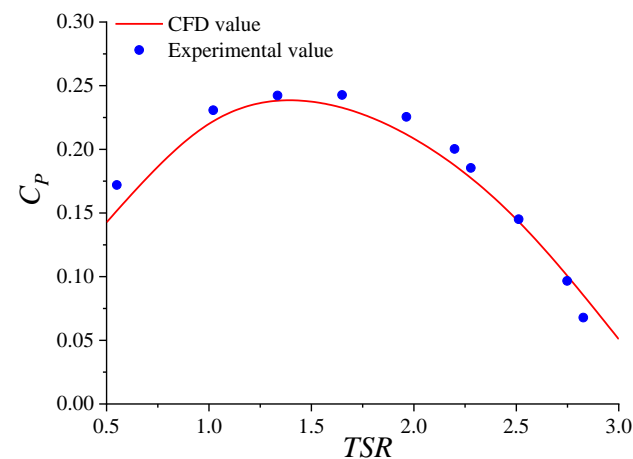

Figure 7. The wind tunnel test system.

Figure 8. Comparison between the experimental value and the CFD value.

3. Results and Discussion

3.1. Power and Thrust

Figure 9 shows the C_P and C_T variation TSR curves for the five ASWT rotors at $V_0 = 5$ m/s. The C_P curves for the five ASWT rotors show a same trend, which rise at first and then fall off. The C_T curves for the five ASWT rotors show a monotonic downward trend with the increase in TSR. Figure 10 shows the maximum C_P and the mean C_T over whole TSR range for the five ASWT rotors. The 30-45-60 has the largest $C_{P\max}$ at TSR of 1.5 among the five ASWT rotors, and the 30-30-30 has the lowest $C_{P\max}$ at TSR of 1.25. The rest of three have a closer $C_{P\max}$. Thus, the $C_{P\max}$ of the five ASWT rotors are all within a range of TSR from 1.0 to 2.0. Additionally, the blade angle can affect the trend in C_P curve. A large blade angle gives the ASWT a wider operating TSR range, and the TSR point of $C_{P\max}$ is shifted to a higher TSR position. For example, the 60-60-60 has the widest operating TSR range, and the TSR point of $C_{P\max}$ is at the highest TSR position among the three fixed-angle ASWT rotors. Additionally, the same situation happens when comparing a fixed-angle ASWT with a variable-angle ASWT, such as comparing 15-30-45 with 45-45-45 or comparing 30-45-60 with 60-60-60. On the other hand, a large blade angle also gives the ASWT a larger $C_{T\mean}$. For example, the 60-60-60 has the largest $C_{T\mean}$ among the three fixed-angle ASWT rotors. Still, when comparing a fixed-angle ASWT with a variable-angle ASWT, such as comparing 15-30-45 with 45-45-45 or comparing 30-45-60 with 60-60-60, it is noted that the ASWT with the larger blade angle has a larger $C_{T\mean}$. Most interestingly, as for the cases where the sum of the blade angle are equal, the $C_{T\mean}$ of 30-45-60 and

45-45-45 are very close, and the $C_{T\text{mean}}$ of 15-30-45 is slightly smaller than that of 30-30-30 due to the fact that its α_0 has brought extra thrust. The above phenomena are mainly due to the different flow effect inside the ASWT blade caused by the blade angle. The ASWT with the smaller blade angle permits the undisturbed free stream to pass through the rotor blade more easily than that of the ASWT with the larger blade angle, as discussed later.
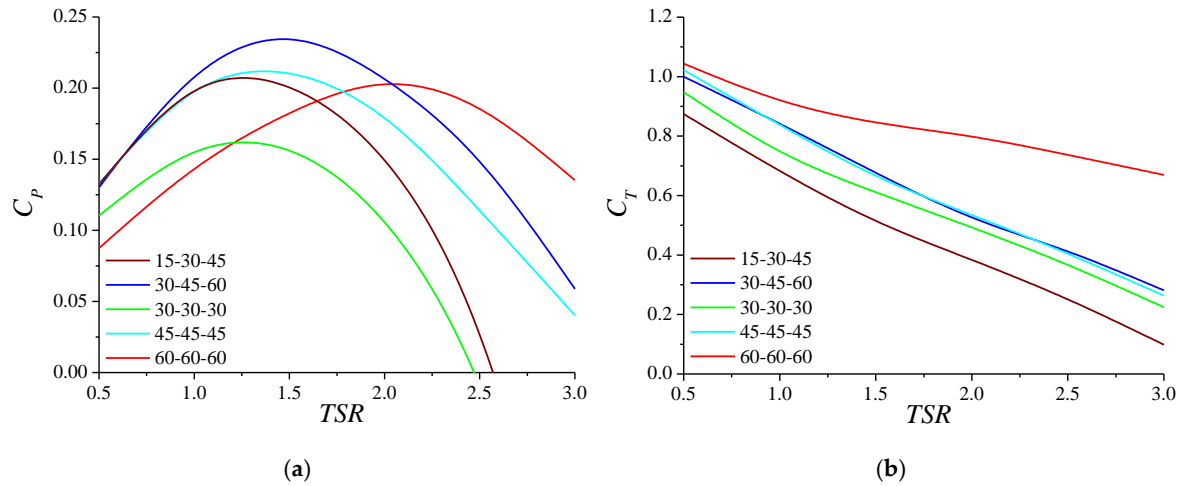

Figure 9. C_P and C_T versus *TSR* for the five ASWT rotors: (**a**) C_P; (**b**) C_T.

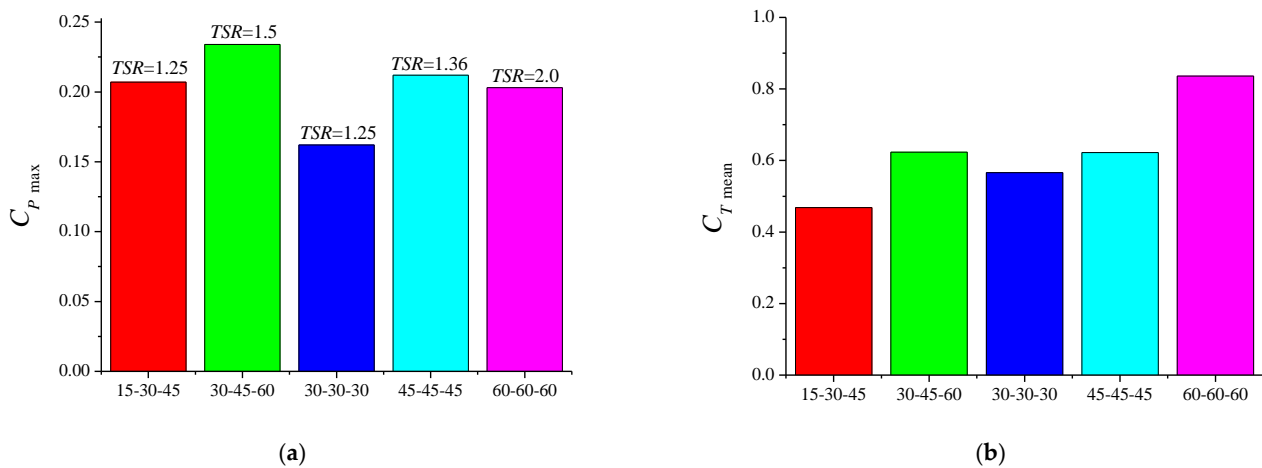**Figure 10.** $C_{P\text{max}}$ and $C_{T\text{mean}}$ for the five ASWT rotors: (**a**) $C_{P\text{max}}$; (**b**) $C_{T\text{mean}}$.

In summary, the ASWT with the larger blade angle has a wider operating *TSR* range and a higher *TSR* point of $C_{P\text{max}}$ within a certain range, and yet the ASWT with the larger blade angle has a higher $C_{T\text{mean}}$. The ASWT rotors are suitable for operation under low wind speed and low *TSR* range conditions, so they generate less aerodynamic noise than other type of wind turbines. Additionally, the ASWT also has higher energy harvesting efficiency than some HAWTs [31] and VAWTs [32] within a certain operation range, which makes it highly fit for an urban environment [33].

3.2. Performance Fluctuation Characteristics

In this and follow-up sections, the results and analysis for the five ASWT rotors at *TSR* = 1.5 are presented. In addition, to illustrate the differences between a single ASWT rotor and a rotor with a tower, the 30-45-60 rotor with a tower is considered as a comparative case. Figure 11 shows the schematic view of the ASWT rotor with a tower.
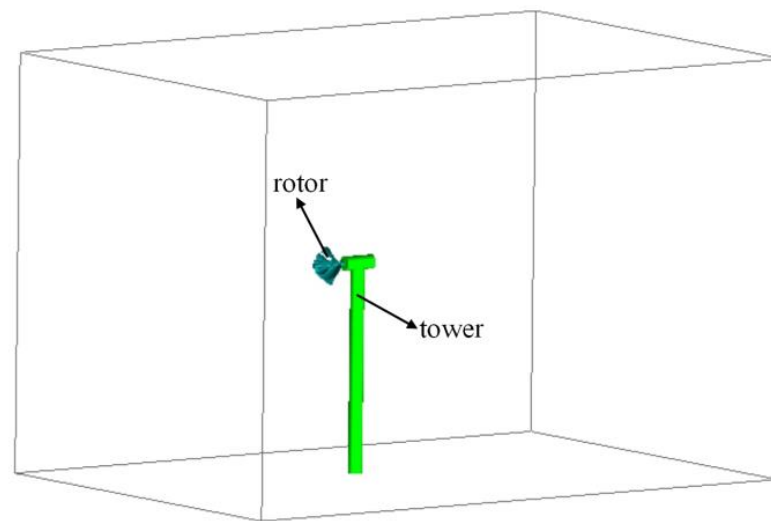
Figure 11. The ASWT rotor with a tower.

Figure 12 shows the C_P and C_T versus time for the five ASWT rotors at $TSR = 1.5$. Figure 13 compares the maximum, mean and minimum values for C_P and C_T. The time series of C_P and C_T for the five ASWT rotors present obvious periodic oscillations and show the same time-periodic behavior due to the fact that the rotational speed is equal. However, there are differences in the fluctuation amplitude of the five ASWT rotors. For the C_P, the fluctuation amplitude ranging in order from the large to the small are: 30-30-30, 30-45-60, 60-60-60, 45-45-45 and 15-30-45. For the C_T, the fluctuation amplitude ranging in order from the large to the small are: 30-30-30, 60-60-60, 30-45-60, 45-45-45 and 15-30-45. Therefore, the ASWT with the larger blade angle has a stronger fluctuation in aerodynamic performance, which may lead to a fatigue problem on ASWT blades. The reason that the 30-30-30 has the maximum fluctuation amplitude among the five ASWT rotors is probably due to the fact that its $\alpha 1$ brings an additional aerodynamic effect. Additionally, compared with the non-tower case, the mean value on C_P and C_T of the tower case has decreased by 2.4% and 2.6%, respectively. The fluctuation amplitude on C_P and C_T has increased by 25.5% and 21.4, respectively.
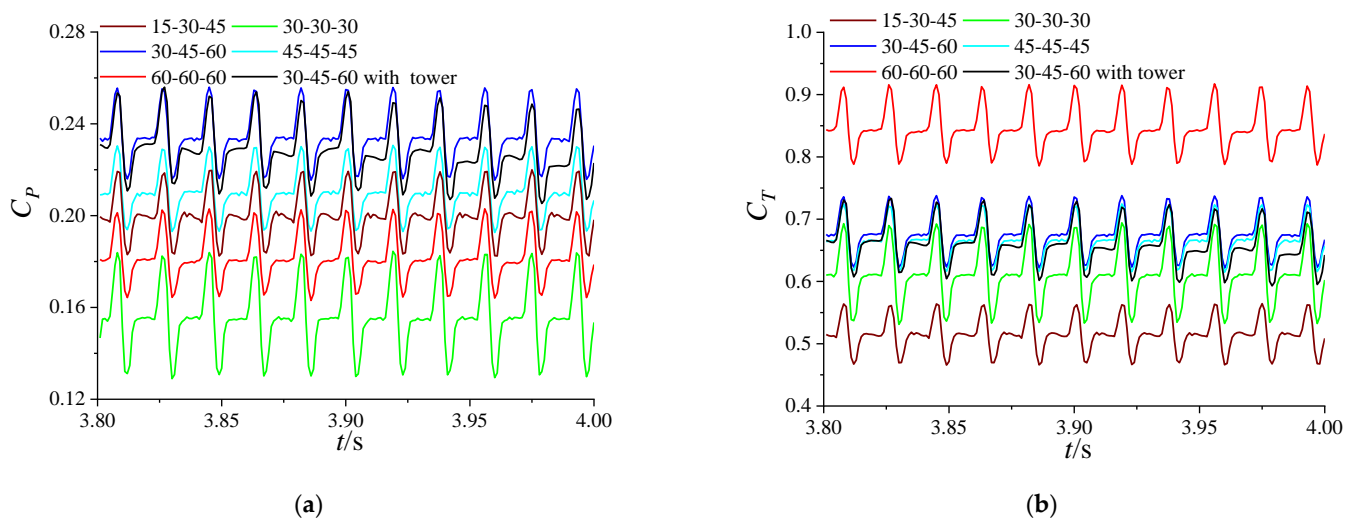

(**a**)

(**b**)

Figure 12. Time histories of C_P and C_T for the five ASWT rotors at TSR = 1.5: (**a**) C_P; (**b**) C_T.
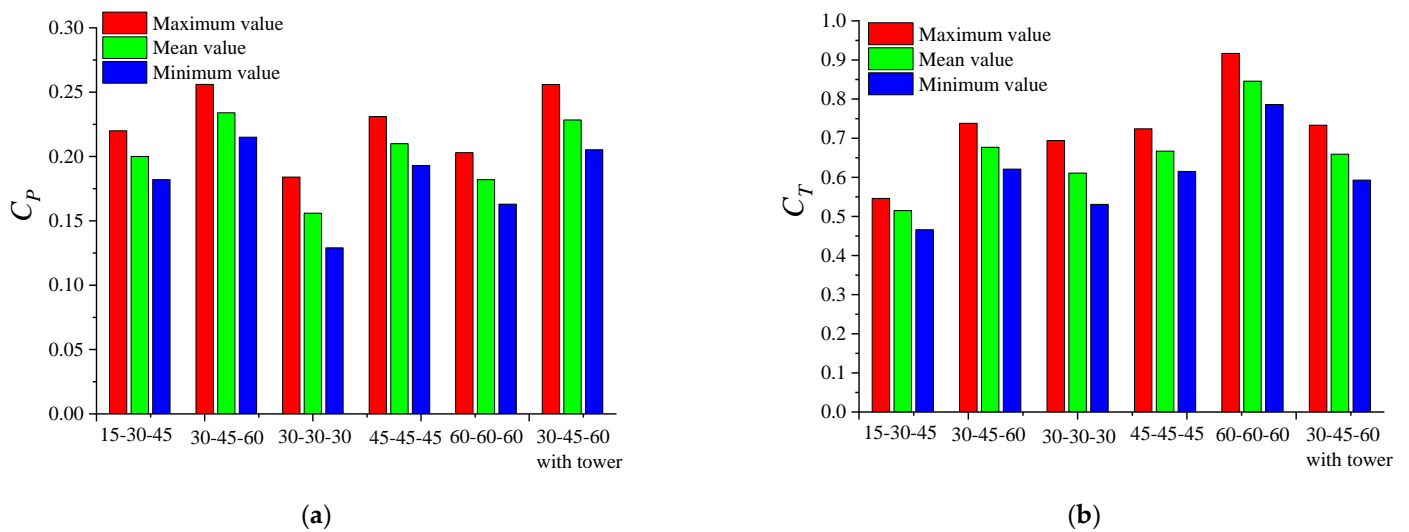
(**a**)

(**b**)

Figure 13. Maximum, minimum, mean C_P and C_T for the five ASWT rotors at $TSR = 1.5$: (**a**) C_P; (**b**) C_T.

3.3. Pressure Distribution on Blade

Figure 14 shows the pressure coefficient (ΔCp) on the five ASWT rotors at $TSR = 1.5$. When an ASWT rotor is rotating, facing the impact of the wind, part of the air kinetic energy can be extracted into mechanical energy like a traditional HAWT. High pressure is created on the pressure side while low pressure is created on the suction side, and the pressure difference leads to torque and thrust. It can be observed that a higher-pressure region of the pressure side and a lower-pressure region of the suction side gradually moved to the blade edge. In addition, as wind passes through the ASWT rotor continuously, a local low-pressure region appears on the end edge of the pressure side on account of the fact that the wind will move across the end edge and create higher velocity. Meanwhile, the pressure on the five ASWT blades is different from each other. It can be seen that the ASWT rotors with a large blade angle have a larger high-pressure region than those with a small blade angle. Moreover, the ΔCp for 30-45-60 with a tower is obviously lower than that of rotors without a tower.

3.4. Velocity Contours and Vortex Structures

The velocity contours (left) and the vortex structures (right) colored by velocity for the five ASWT rotors at $TSR = 1.5$ are shown in Figure 15. When wind streams move across the ASWT rotors, the velocity in the wake region reduces significantly due to the block effect. In this process, the rotation of the rotor is followed by a velocity decrease in the wake, and the streamwise momentum is converted to the angular momentum. In addition, the highest velocity region is observed near the blade tip, while the lowest velocity region is observed behind the hub, so the turbulence generation would be obvious in these regions. Furthermore, owing to the difference in blade angle, the velocity contours of each ASWT are quite different. The low velocity region size of 60-60-60 is much larger than the other four ASWT rotors; especially, the hub recirculation region is quite distinguishable. As mentioned above, a different blade angle causes a different flow effect inside the ASWT blade; the ASWT with a small blade angle permits the undisturbed free stream to pass through the rotor blade more easily than that with a large blade angle. Therefore, the ASWT with a large blade angle has a stronger blockage effect than the ASWT with a small blade angle.
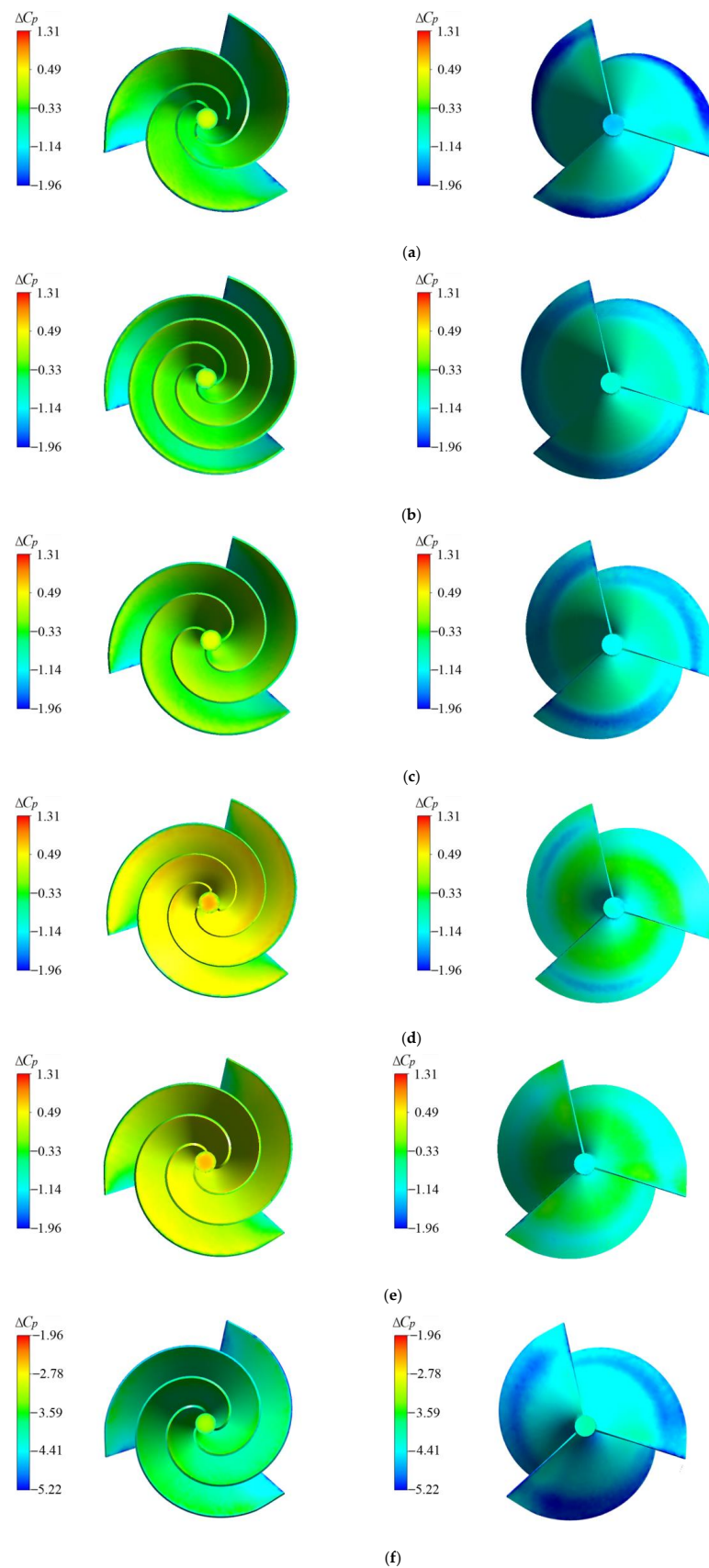
Figure 14. Pressure coefficient ($\Delta C_p = \frac{p}{0.5\rho V_0^2}$) distribution on the five ASWT rotors at $TSR = 1.5$, pressure side (**left**) and suction sides (**right**): (**a**) 15-30-45; (**b**) 30-30-30; (**c**) 45-45-45; (**d**) 60-60-60; (**e**) 30-45-60; (**f**) 30-45-60 with tower.
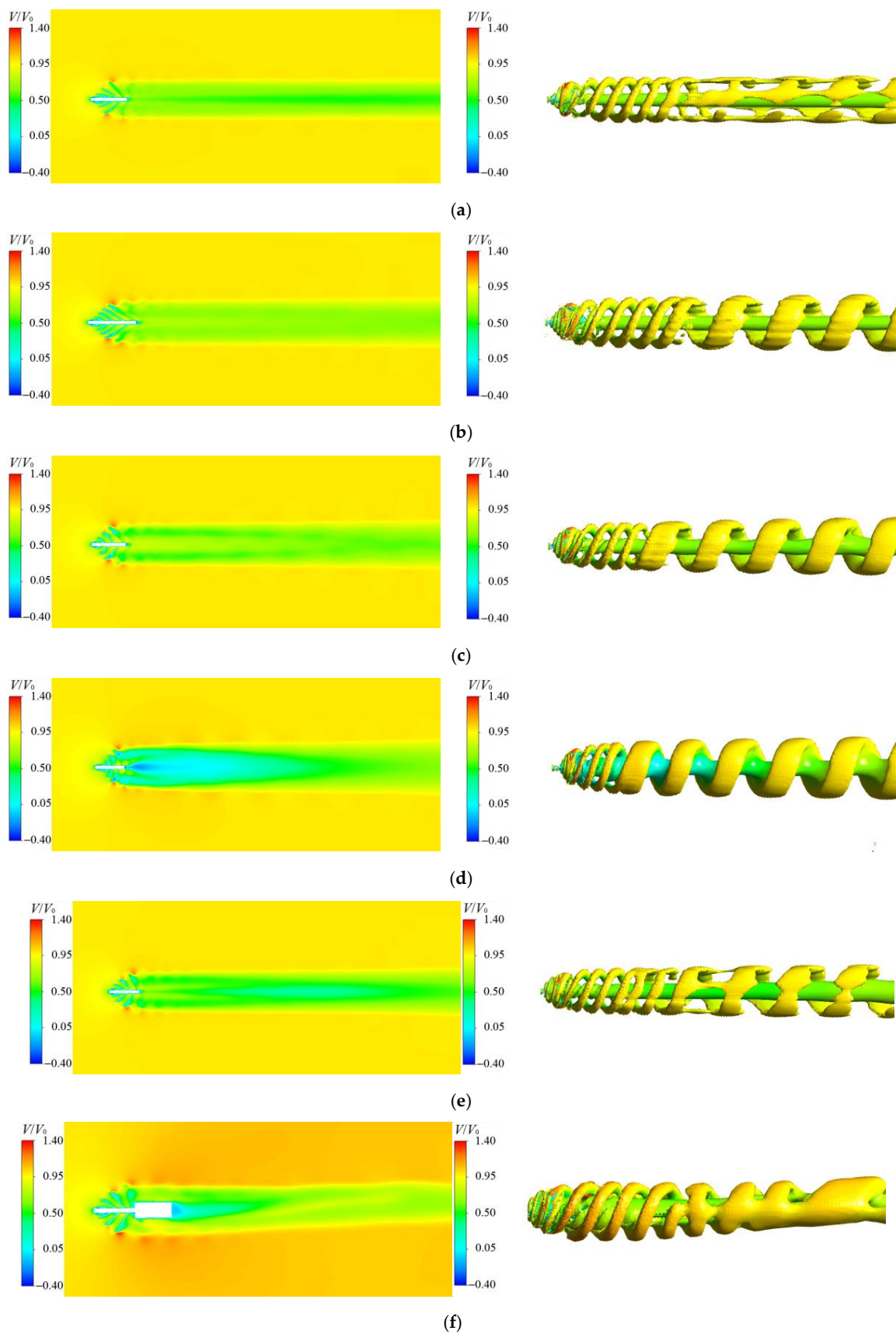
Figure 15. Velocity contours (**left**) and vortex structures colored by velocity (**right**) for the five ASWT rotors at $TSR = 1.5$ in the central *x-z* plane: (**a**) 15-30-45; (**b**) 30-30-30; (**c**) 45-45-45; (**d**) 60-60-60; (**e**) 30-45-60; (**f**) 30-45-60 with tower.

A large-scale vortex shedding from the blade tip and hub of the ASWT rotor is observed in the right side of Figure 15.However, the tip vortex structure of the ASWT is a little different from that generated by the conventional HAWT [34–36]. Due to the spiral shape of an ASWT rotor, the airflow speed through the blade surface is high, which makes the tip vortex strong and develop in a long spiral pattern along the downstream direction [14]. Furthermore, there are certain differences between the five ASWT rotors' vortex structures, as we can see by comparing the vortex structures. The blade angle has a great effect on the shape of the vortex structure. The tip vortex of 30-30-30, 45-45-45 and 60-60-60 has clearly extended to a longer distance before scattering into a shattered pattern than those of 15-30-45 and 30-45-60. These phenomena suggest that the tip vortex of the fixed-angle rotors is more stable than those of the variable-angle ones. Moreover, the hub vortex of 60-60-60, 30-45-60 and 45-45-45 is stronger than those of 30-30-30 and 15-30-45. Especially, the hub vortex of 60-60-60 has mixed together with the tip vortex. These phenomena suggest that the hub vortex of the ASWT rotors with a large blade angle is stronger than those with a small blade angle.

3.5. Velocity Profiles and Turbulence Intensity

The velocity profiles (left) and the turbulence intensity (right) in the central x-z plane at selected downstream distances (z/D = 1, 3, 5 and 10) for the five ASWT rotors at $TSR = 1.5$ are shown in Figure 16. Overall, the velocity profiles are almost symmetric along the ASWT rotor axis, which show a gradually recovery trend as the flow travels downstream. The turbulence intensity exhibited sharp corners at x/D = ±0.5 for the five ASWT rotors. This means that a high level of turbulence occurred at this location, which is due to the formation of the tip vortex and its periodical shedding. Furthermore, there is a divergence in the wake recovery for the five ASWT rotors. It is very interesting that the 60-60-60 has the highest turbulence intensity and its wake recovery rate is faster than the other ASWT rotors. It seems that the higher the turbulence intensity is, the faster the wake recovery is. This is due to enhanced turbulent mixing in the wake and its momentum being transferred [37]. Meanwhile, the wake recovery for the other four ASWT rotors is evidently lower than the 60-60-60, especially for those with a small blade angle like 30-30-30 and 15-30-45.

On the other hand, Figures 15 and 16 also indicate that considering the tower, the velocity reduction on the one side is more than that on the other side, due to the fact that the tower causes the asymmetric distribution of velocity in the wake region. The rotating velocity induced by the ASWT rotor can be easily arrested and attenuated by the tower, which makes the wake recover more easily. Additionally, the rotating ASWT rotor leads to flow stagnation on the other side of the tower. Thus, an asymmetric distribution of the velocity and the vortex structure is found. It is worth mentioning that the wake interaction between the ASWT rotor and the tower are much more complicated than we discuss in the current work.
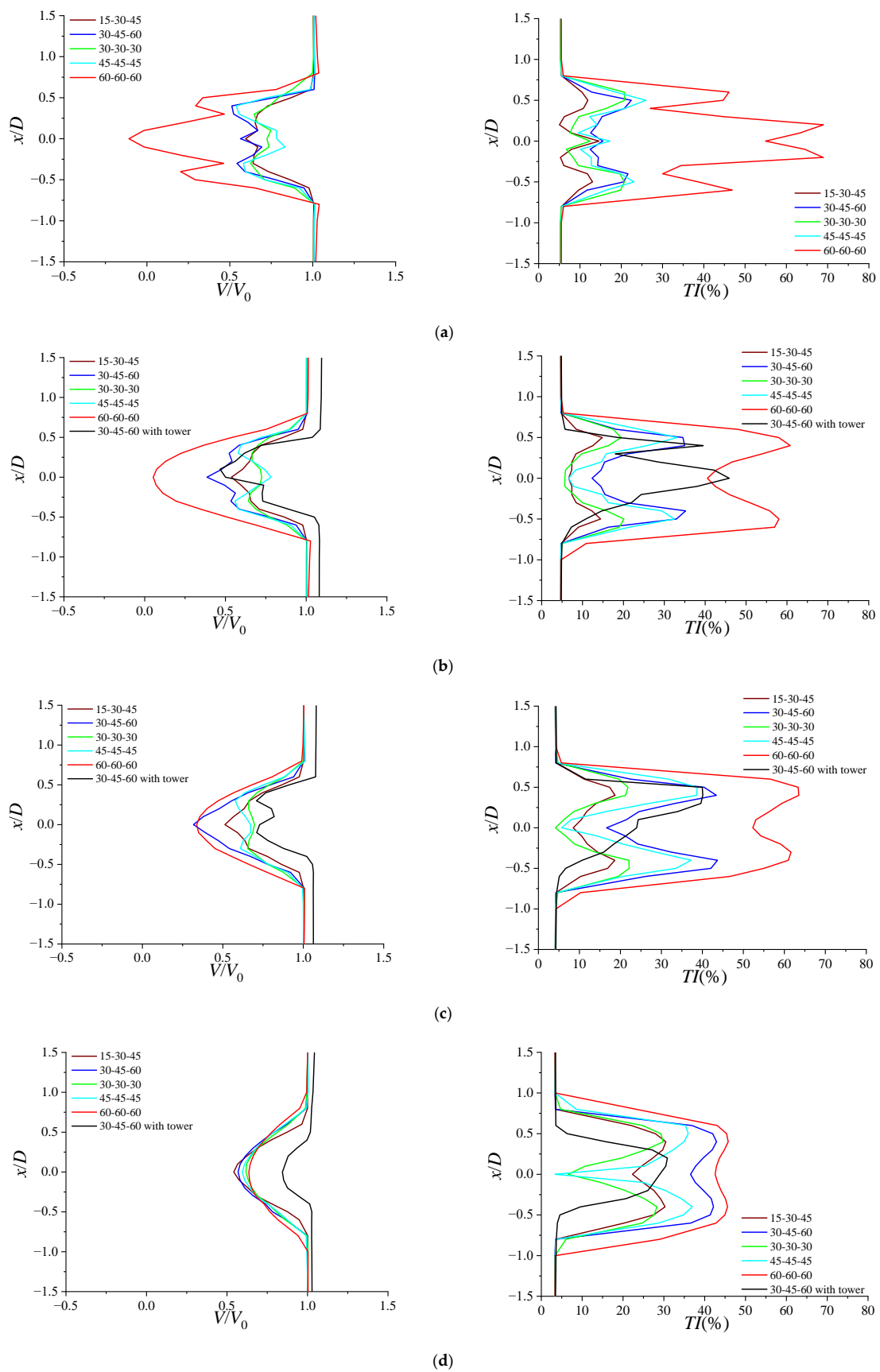
Figure 16. Profiles of velocity (**left**) and turbulence intensity (**right**) for the five ASWT rotors at $TSR = 1.5$ in the central x-z plane: (**a**) $z/D = 1.0$; (**b**) $z/D = 3.0$; (**c**) $z/D = 5.0$; (**d**) $z/D = 10.0$.

4. Conclusions

In the present work, the application of a new type of wind turbine, namely the ASWT, was investigated using CFD. The detailed aerodynamic performance and wake characteristics of five ASWT rotors with different blade angles, including the variation of power, thrust, pressure distribution, velocity distribution and the vortex structures, were conducted to investigate. Some important findings have been concluded from this study as follows:

The 30-45-60 has the largest $C_{P\max}$ of 0.234 at TSR of 1.5 among the five ASWT rotors. The $C_{P\max}$ of the five ASWT rotors are all within a range of TSR from 1.0 to 2.0, which indicates that the ASWT rotors are suitable for operation under low wind speed and low TSR range conditions. Additionally, the ASWT rotor with a larger blade angle has a wider operating TSR range and a higher TSR point of $C_{P\max}$ within a certain range, and yet the ASWT rotor with a larger blade angle has a higher $C_{T\mathrm{mean}}$. Moreover, the ASWT rotor with a larger blade angle has a stronger fluctuation in aerodynamic performance, which may lead to a fatigue problem on ASWT blades. Compared with the non-tower case, the tower has led to a decrease in the mean value and an amplification of the fluctuation amplitude in C_P and C_T.

A different blade angle causes different flow effects inside the ASWT blade; the ASWT rotor with a small blade angle permits the undisturbed free stream to pass through the blade more easily than that with a large blade angle. Therefore, the ASWT rotor with a large blade angle has a stronger blockage effect than that with a small blade angle, and the stronger blockage effect forces more fluid go through the region near the hub. On the other hand, there is a large-scale vortex structure, which sheds from the blade tip and hub of the ASWT rotors. The blade angle has a great effect on the shape of the vortex structure. The tip vortex of the fixed-angle rotors is more stable than those of the variable-angle ones. The hub vortex of the ASWT rotors with a large blade angle is stronger than that of those with a small blade angle. Furthermore, the 60-60-60 rotor has the highest turbulence intensity, and its wake recovery rate is faster than the other ASWT rotors. It seems that the higher the turbulence intensity is, the faster the wake recovery is. This is due to enhanced turbulent mixing in the wake and its momentum being transferred. Meanwhile, the wake recovery for the other four ASWT rotors is evidently lower than the 60-60-60, especially for the ASWT rotors with a small blade angle such as 30-30-30 and 15-30-45. The velocity and vortex structure are asymmetric along the ASWT rotor axis when the tower is being considered, which may be caused by the rotor–tower wake interaction.

A few works on the ASWT have been introduced for the time being; some aspects have not been studied much yet, which we will carry out in our future works. For example, performance improvement based on blade angle optimization is one of the future works we have planned. Additionally, the blade section effect caused by rotational augmentation is also a future work. This has been investigated a lot for HAWT [38–40] but no significant effort has been spent on studying this effect in ASWTs. Moreover, the mechanism of the rotor–tower interaction, caused by flow separation, dynamic stall, turbulence, yaw effect and so on, is another future work. This also has been investigated a lot for HAWT [41–44] but not for ASWTs.

Author Contributions: Conceptualization, K.S.; methodology, K.S. and Y.K.; software, H.H. and Y.K.; validation, H.H.; formal analysis, K.S.; investigation, K.S.; resources, K.S.; data curation, K.S.; writing—original draft preparation, K.S.; writing—review and editing, K.S. and H.H.; visualization, Y.K.; supervision, K.S.; project administration, K.S.; funding acquisition, K.S. All authors have read and agreed to the published version of the manuscript.

Institutional Review Board Statement: Not applicable.

Informed Consent Statement: Not applicable.

Data Availability Statement: Not applicable.

Conflicts of Interest: The authors declare no conflict of interest.

References

1. Enevoldsen, P.; Valentine, S.V.; Sovacool, B.K. Insights into wind sites: Critically assessing the innovation, cost, and performance dynamics of global wind energy development. *Energy Policy* **2018**, *120*, 1–7. [CrossRef]
2. Rand, J.; Hoen, B. Thirty years of North American wind energy acceptance research: What have we learned? *Energy Res. Soc. Sci.* **2017**, *29*, 135–148. [CrossRef]
3. Barthelmie, R.J.; Pryor, S.C. The impact of wind direction yaw angle on cliff flows. *Wind Energy* **2018**, *21*, 1254–1265. [CrossRef]
4. Ciri, U.; Rotea, M.A.; Leonardi, S. Effect of the turbine scale on yaw control. *Wind Energy* **2018**, *21*, 1395–1405. [CrossRef]
5. Bader, S.H.; Inguva, V.; Perot, J.B. Improving the efficiency of wind farms via wake manipulation. *Wind Energy* **2018**, *21*, 1239–1253. [CrossRef]
6. Porté-Agel, F.; Bastankhah, M.; Shamsoddin, S. Wind-turbine and wind-farm flows: A review. *Bound-Lay Meteorol.* **2020**, *174*, 1–59. [CrossRef]
7. Johari, M.K.; Jalil, M.; Shariff, M.F.M. Comparison of horizontal axis wind turbine (HAWT) and vertical axis wind turbine (VAWT). *Int. J. Eng. Tech.* **2018**, *7*, 74–80. [CrossRef]
8. Karthikeyan, N.; Murugavel, K.K.; Kumar, S.A.; Rajakumar, S. Review of aerodynamic developments on small horizontal axis wind turbine blade. *Renew. Sustain. Energy Rev.* **2015**, *42*, 801–822. [CrossRef]
9. Rehman, S.; Alam, M.M.; Alhems, L.M.; Rafique, M.M. Horizontal axis wind turbine blade design methodologies for efficiency enhancement—A review. *Energies* **2018**, *11*, 506. [CrossRef]
10. Castellanos Bustamante, R.; Roman Messina, A.; Ramirez Gonzalez, M.; Calderon Guizar, G. Assessment of frequency performance by wind integration in a large-scale power system. *Wind Energy* **2018**, *21*, 1359–1371. [CrossRef]
11. Murali, A.; Rajagopalan, R.G. Numerical simulation of multiple interacting wind turbines on a complex terrain. *J. Wind Eng. Ind. Aerod.* **2017**, *162*, 57–72. [CrossRef]
12. Ji, H.S.; Baek, J.H.; Mieremet, R.; Kim, K.C. The aerodynamic performance study on small wind turbine with 500W class through wind tunnel experiments. *Int. J. Renew. Energy Sources* **2016**, *1*, 7–12.
13. Rao, S.S.; Shanmukesh, K.; Naidu, M.K.; Kalla, P. Design and Analysis of Archimedes Aero-Foil Wind Turbine Blade for Light and Moderate Wind Speeds. *Int. J. Recent Technol. Mech. Electr. Eng.* **2018**, *5*, 1–5.
14. Kim, K.; Ji, K.; Kim, H.Y.; Lu, Q.; Baek, J. Experimental and Numerical Study of the Aerodynamic Characteristics of an Archimedes Spiral Wind Turbine Blade. *Energies* **2014**, *7*, 7893–7914. [CrossRef]
15. Safidari, A.; Kim, K.C. Aerodynamic and Structural Evaluation of Horizontal Archimedes Spiral Wind Turbine. *J. Clean Energy Technol.* **2015**, *3*, 34–38. [CrossRef]
16. Lu, Q.; Li, Q.; Kim, Y.K.; Kim, K.C. A study on design and aerodynamic characteristics of a spiral-type wind turbine blade. *J. Korean Soc. Vis.* **2012**, *10*, 27–33.
17. Jang, H.; Kim, D.; Hwang, Y.; Paek, I.; Kim, S.; Baek, J. Analysis of Archimedes spiral wind turbine performance by simulation and field test. *Energies* **2019**, *12*, 4624. [CrossRef]
18. Nawar, M.A.; Hameed, H.A.; Ramadan, A.; Attai, Y.A.; Mohamed, M.H. Experimental and numerical investigations of the blade design effect on Archimedes Spiral Wind Turbine performance. *Energy* **2021**, *223*, 120051. [CrossRef]
19. Kamal, A.M.; Nawar, M.A.; Attai, Y.A.; Mohamed, M.H. Archimedes Spiral Wind Turbine performance study using different aerofoiled blade profiles: Experimental and numerical analyses. *Energy* **2023**, *262*, 125567. [CrossRef]
20. Kamal, A.M.; Nawar, M.A.; Attai, Y.A.; Mohamed, M.H. Blade design effect on Archimedes Spiral Wind Turbine performance: Experimental and numerical evaluations. *Energy* **2022**, *250*, 123892. [CrossRef]
21. Sapkota, S.; Bhattarai, A.; Bashyal, H.P.; Nepal, U. Design, CFD analysis and modelling of archimedean-spiral type wind turbine. *Proc. IOE Grad.Conf.* **2019**, *6*, 563–571.
22. Mustafa, A.T.; Jaleel, H.A. A comparison study between Archimedes spiral turbine and propeller turbine with wind attack angle effect. *AIP Conf. Proc.* **2020**, *2213*, 020058.
23. Ozeh, M.; Mishra, A.; Wang, X. Mini wind turbine for small scale power generation and storage (Archimedes wind turbine model). In *Proceedings of the ASME International Mechanical Engineering Congress and Exposition*; American Society of Mechanical Engineers: Pittsburgh, PA, USA, 2018.
24. Refaie, A.G.; Hameed, H.A.; Nawar, M.A.; Attai, Y.A.; Mohamed, M.H. Comparative investigation of the aerodynamic performance for several Shrouded Archimedes Spiral Wind Turbines. *Energy* **2022**, *239*, 122295. [CrossRef]
25. Hameed, H.S.A.; Hashem, I.; Nawar, M.A.; Attai, Y.A.; Mohamed, M.H. Shape optimization of a shrouded Archimedean-spiral type wind turbine for small-scale applications. *Energy* **2023**, *263*, 125809. [CrossRef]
26. Menter, F.R. Two-equation eddy-viscosity turbulence models for engineering applications. *AIAA J.* **1994**, *32*, 1598–1605. [CrossRef]
27. Rocha, P.C.; Rocha, H.B.; Carneiro, F.M.; Da Silva, M.V.; Bueno, A.V. k–ω SST (shear stress transport) turbulence model calibration: A case study on a small scale horizontal axis wind turbine. *Energy* **2014**, *65*, 412–418. [CrossRef]

28. Rezaeiha, A.; Montazeri, H.; Blocken, B. On the accuracy of turbulence models for CFD simulations of vertical axis wind turbines. *Energy* **2019**, *180*, 838–857. [CrossRef]

29. Song, K.; Yang, B. A Comparative Study on the Hydrodynamic-Energy Loss Characteristics between a Ducted Turbine and a Shaftless Ducted Turbine. *J. Mar. Sci. Eng.* **2021**, *9*, 930. [CrossRef]

30. Song, K.; Kang, Y. A Numerical Performance Analysis of a Rim-Driven Turbine in Real Flow Conditions. *J. Mar. Sci. Eng.* **2022**, *10*, 1185. [CrossRef]

31. Bai, C.J.; Wang, W.C. Review of computational and experimental approaches to analysis of aerodynamic performance in horizontal-axis wind turbines (HAWTs). *Renew. Sustain. Energy Rev.* **2016**, *63*, 506–519. [CrossRef]

32. Mu, Z.; Tong, G.; Xiao, Z.; Deng, Q.; Feng, F.; Li, Y.; Arne, G.V. Study on aerodynamic characteristics of a Savonius wind turbine with a modified blade. *Energies* **2022**, *15*, 6661. [CrossRef]

33. Howell, R.; Qin, N.; Edwards, J.; Durrani, N. Wind tunnel and numerical study of a small vertical axis wind turbine. *Renew. Energy* **2010**, *35*, 412–422. [CrossRef]

34. Arabgolarcheh, A.; Jannesarahmadi, S.; Benini, E. Modeling of near wake characteristics in floating offshore wind turbines using an actuator line method. *Renew. Energy* **2022**, *185*, 871–887. [CrossRef]

35. Fang, Y.; Li, G.; Duan, L.; Han, Z.; Zhao, Y. Effect of surge motion on rotor aerodynamics and wake characteristics of a floating horizontal-axis wind turbine. *Energy* **2021**, *218*, 119519. [CrossRef]

36. Lee, H.; Lee, D.J. Effects of platform motions on aerodynamic performance and unsteady wake evolution of a floating offshore wind turbine. *Renew. Energy* **2019**, *143*, 9–23. [CrossRef]

37. Kabir, I.F.S.A.; Ng, E.Y.K. Effect of different atmospheric boundary layers on the wake characteristics of NREL phase VI wind turbine. *Renew. Energy* **2019**, *130*, 1185–1197. [CrossRef]

38. Bangga, G.; Lutz, T.; Jost, E.; Krämer, E. CFD studies on rotational augmentation at the inboard sections of a 10 MW wind turbine rotor. *J. Renew. Sustain. Energy* **2017**, *9*, 023304. [CrossRef]

39. Bangga, G. *Three-Dimensional Flow in the Root Region of Wind Turbine Rotors*; Kassel University Press GmbH: Kassel, Germany, 2018.

40. Schreck, S.; Robinson, M. Boundary layer state and flow field structure underlying rotational augmentation of blade aerodynamic response. *J. Sol. Energy Eng.* **2003**, *125*, 448–456. [CrossRef]

41. Bangga, G.; Hutomo, G.; Wiranegara, R.; Sasongko, H. Numerical study on a single bladed vertical axis wind turbine under dynamic stall. *J. Mech. Sci. Technol.* **2017**, *31*, 261–267. [CrossRef]

42. Bangga, G. Numerical studies on dynamic stall characteristics of a wind turbine airfoil. *J. Mech. Sci. Technol.* **2019**, *33*, 1257–1262. [CrossRef]

43. Fujisawa, N.; Shibuya, S. Observations of dynamic stall on Darrieus wind turbine blades. *J. Wind Eng. Ind. Aerodyn.* **2001**, *89*, 201–214. [CrossRef]

44. Simão Ferreira, C.; Van Kuik, G.; Van Bussel, G.; Scarano, F. Visualization by PIV of dynamic stall on a vertical axis wind turbine. *Exp. Fluids* **2009**, *46*, 97–108. [CrossRef]